2

Coherent X-rays

2.1 Definitions of coherence

In coherence theory, two types of coherence are discussed: longitudinal and transverse coherence. Longitudinal coherence is a wave's property of interfering with a *time-delayed* copy of itself. Longitudinally coherent light will produce fringes in a Michelson interferometer until its two mirrors are separated from each other by a distance much larger than the longitudinal coherence length [38] given by

$$l_l \approx \lambda^2/2\delta\lambda, \tag{2.1}$$

where λ is the wavelength of the light, and $\delta\lambda/\lambda$ is the relative bandwidth of the source. Eq. 2.1 follows from the Heisenberg uncertainty principle $\delta\nu\tau_l \approx 1$, where $\delta\nu$ is the frequency bandwidth of the light and $c\tau_l = l_l$, where c is the speed of light in vacuum. Stated physically, the longitudinal coherence length is the characteristic length along the direction of propagation of a wave packet emitted by a given polychromatic source. For a monochromatic wave, l_l is infinite. For a constant relative bandwidth $\delta\lambda/\lambda$, l_l is proportional to the wavelength used.

A wave is called transversely coherent if it can produce fringes in a Young's double-slit experiment. The transverse coherence length l_t characterizes the loss of coherence or of fixed phase relationship between two points on a wavefront. In a Young's double-slit experiment, no interference fringes are seen [38] if the two slits are separated by a distance d much larger than the transverse coherence length

$$l_t = \lambda R_s/2d_s = \lambda/2\alpha, \tag{2.2}$$

where R_s is the source to observation point distance, d_s is the source size, and $\alpha = d_s/R_s$ is the opening angle subtended by the source at the point of observation. Stated in another fashion, if one places two pinholes separated by $d < l_t$ in front of an extended source, the interference patterns generated by each element of the source overlap each other, thus interference is visible. For a point source, the transverse coherence length diverges. For an extended source, l_t increases with increasing λ, making it easier to observe interference effects at longer wavelengths. The transverse coherence length is also inversely proportional to the opening angle subtended by the source at the point of observation.

Formally, a source is coherent when there is a non-zero statistical correlation between electric fields $\vec{E}(r_1, t_1)$ and $\vec{E}(r_2, t_2)$. The mutual coherence function is defined by

$$\Gamma_{12} = <\vec{E}^*(r_1, t_1)\vec{E}(r_2, t_2)>_t, \tag{2.3}$$

where the average is taken over time.

It can be shown [39] that the mutual coherence function far away from an **incoherent source** made of independent radiators[1] simplifies to the spatial Fourier transform of the source intensity profile. Then the complex coherence factor

$$\mu(\vec{r}_1, \vec{r}_2) = \frac{e^{\frac{-\pi i(r_2^2 - r_1^2)}{\lambda R_s}} \int_{-\infty}^{\infty}\int_{-\infty}^{\infty} dx'dy' I(\vec{r}') \exp(\frac{2\pi i}{\lambda R_s}\vec{r}' \cdot (\vec{r}_2 - \vec{r}_1))}{\int_{-\infty}^{\infty}\int_{-\infty}^{\infty} dx'dy' I(\vec{r}')}, \tag{2.4}$$

where the vector $\vec{r}'$ is a small vector in the source plane, λ is the average wavelength of the source, and $\vec{r}_1$ and $\vec{r}_2$ are two vectors in the plane of observation perpendicular to the optical axis of the source and placed at a distance R_s from the source. This is called the Van Cittert-Zernicke theorem. It holds for small angles of observation such that the transverse distance $|\vec{r}_2 - \vec{r}_1| << R_s$, and under quasi-monochromatic conditions. This theorem is very useful because it can be used to calculate the fringe contrast in a Young's double-slit experiment [39] for most light sources.

[1]This assumption characterizes nearly all optical sources other than a laser. It can be applied to synchrotron radiation.

Following Goodman [39], we define the coherence area by

$$A_c = \int_{-\infty}^{\infty} \int_{-\infty}^{\infty} dx'dy' |\mu(x', y')|^2. \tag{2.5}$$

For an incoherent source with a *spatially uniform* intensity profile, it can be shown [39] using the Van Cittert-Zernicke theorem that the coherence area in Eq. 2.5 reduces to the product of the two perpendicular transverse coherence lengths of the source defined in Eq. 2.2. Eq. 2.5 will be used in section 5.1.2 to calculate the observed contrast of our diffraction patterns.

2.2 Properties of synchrotron radiation

The use of synchrotron radiation over the past thirty years has revolutionized the field of X-ray scattering. Today's range of scientific activities in the X-ray scattering community would not be as rich and varied without the use of synchrotron radiation[1]. This radiation has several properties which make it ideal for experiments in physics, chemistry, biology, medicine, engineering, material science and in the development of new drugs and technologies. The photon energy available at a synchrotron ranges from the infrared to gamma rays. No other single source is able to cover such a wide band of energies. This energy can be easily selected for a given system by the use of monochromators and gratings, with a wide range of energy bandpass, $\delta E/E$, typically between 10^{-2} to 10^{-4}. The major improvement over standard laboratory sources is the huge increase in intensity, allowing studies of time dependent dynamics and spectroscopies on a wide range of time scales ($10^{-12} - 10^{4}$ s), or studies of scattering from sample volumes as small as $1(\mu\text{m})^3$ (10^{11} atoms!), weak scatterers like light elements, surfaces and interfaces a few monolayers thick, nuclear charge, or magnetic moments. The source divergence is quite small due to the radiation cone which is shrunk to an opening angle of $1/\gamma$, where $\gamma = E/m_0c^2$, m_0c^2 is the rest mass of the electron or positron, and E is its total energy in the laboratory frame. Furthermore, the source size is small. These two properties yield a large coherent flux which can be

[1] For an introduction to synchrotron radiation, the reader is referred to recent books on the subject [40, 41].

used in coherent X-ray scattering experiments and X-ray holography. The incident X-ray polarization can be controlled to produce linear, circular or elliptical polarizations. This allows for resonant and non-resonant magnetic X-ray scattering, or circular dichroism. Finally, the beam is pulsed, which allows for different spectroscopies and excitation modes to be studied.

The X-ray sources used in this work were insertion devices. An insertion device is a periodic magnetic structure inserted in a straight part of the synchrotron ring. These devices cause the electron orbit to oscillate as a sine wave. The X-rays generated by these oscillations are linearly polarized in the plane of the orbit. Most scattering experiments using synchrotron radiation use a vertical scattering plane to reduce polarization losses [26].

These sources are characterized by a large brilliance or brightness, B, defined as the flux of photons per unit of phase space, which is the flux of photons per unit of source area per unit of solid angle measured in photons/s/mm^2/mrad^2/0.1%BW, where BW stands for the X-ray bandwidth $\delta\lambda/\lambda$. For many optical transformations, the brightness is an invariant. For example, a mirror can be used to focus the X-ray beam to a small spot size, but the beam divergence is increased in proportion, thus the product of the spot size times the beam divergence is conserved. In practice, the brightness may be lost in absorption by windows, or in optical aberration on optical elements like mirrors and monochromators.

An insertion device is characterized by a deflection parameter

$$K = \alpha\gamma = eB\lambda_0/(2\pi m_0 c^2) \approx 0.934 B(T)\lambda_0(cm), \tag{2.6}$$

where α is the maximum deflection angle of the electron trajectory with respect to the axis of the insertion device. This angle characterizes the deflection of the electron trajectory by the periodic magnetic field B with laboratory frame period λ_0[40]. An insertion device with $K > 1$ is called a wiggler while one with $K < 1$ is called an undulator.

A wiggler has a very broad energy spectrum similar to a bending magnet spectrum [41]. Because the angular deviation caused by a wiggler is quite large compared to the angular cone of the emitted synchrotron radiation, the radiation emitted from different periods of the wiggler adds incoherently. Therefore, the peak intensity is proportional to the number of magnetic periods N. This device has more operational freedom than a bending magnet because the magnetic field can be made as large as necessary without changing the electron orbit.

The radiation emitted by an undulator is quite different from wiggler radiation because the radiation emitted from a given period adds coherently with the radiation generated at a later time at the subsequent period [41]. The brightness is proportional to N^2, and its spectrum is peaked around well defined wavelengths called harmonics, functions of λ_0 [41]. The wavelengths of these harmonics along a direction parallel to the plane of the orbit are

$$\lambda_n = \frac{\lambda_0}{2n\gamma^2}(1 + \frac{K^2}{2}), \tag{2.7}$$

where $n = 1, 2, 3...$ [41], and their relative wavelength spread is

$$\frac{\delta\lambda}{\lambda} = \frac{1}{nN}. \tag{2.8}$$

With current undulator designs, the relative bandwidth of a given undulator harmonic is typically in the range of a few percent.

2.3 X-ray scattering

In an X-ray scattering experiment, one measures the differential cross-section of X-rays coherently scattered by the electrons in the material. Using the first Born approximation, the X-ray differential cross-section

$$\frac{d\sigma}{d\Omega} = \Phi_s / I_i \propto S(\vec{q}, t), \tag{2.9}$$

where Φ_s is the scattering rate measured in a solid angle $d\Omega$ subtended by the detector, I_i is the incident intensity, and the structure factor is

$$S(\vec{q}, t) = |\rho(\vec{q}, t)|^2, \text{ where } \rho(\vec{q}, t) = \int d\vec{r} \rho(\vec{r}, t) e^{-i\vec{q}\cdot\vec{r}}. \tag{2.10}$$

Here $\rho(\vec{q}, t)$ is the Fourier transform of the electronic density, $\rho(\vec{r}, t)$, and $\vec{q} \equiv \vec{k}_f - \vec{k}_i$, where $\vec{k}_f$ and $\vec{k}_i$ are respectively the wavevectors of the scattered and incident X-rays

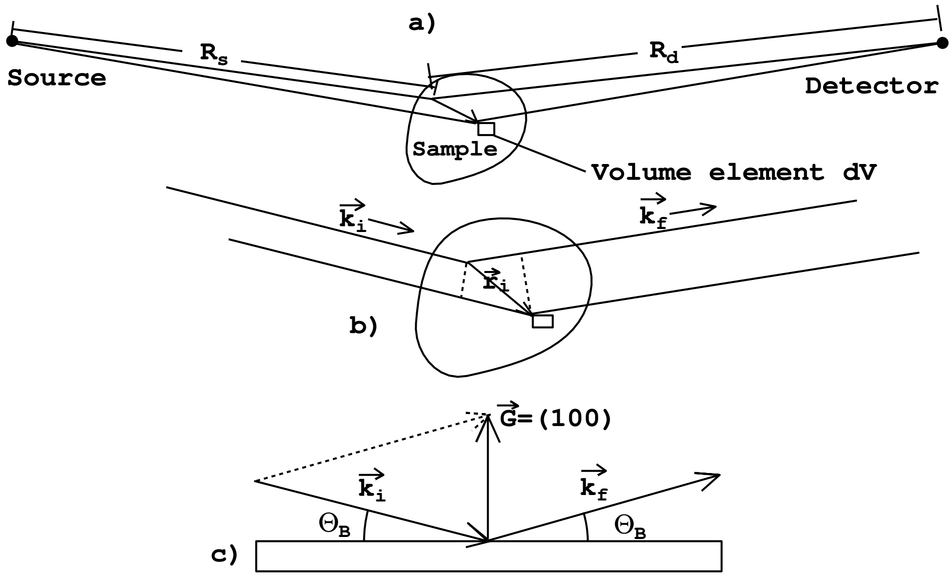

Figure 2.1: a) The Fraunhofer condition holds for plane wave illumination such that the distance source-sample R_s and the distance sample-detector R_d are much larger than the sample size. b) The phase difference, in the Fraunhofer condition. The phase difference $\delta = \vec{k}_f \cdot \vec{r}_i - \vec{k}_i \cdot \vec{r}_i$, where the magnitude of the incident and scattered wavevectors $|\vec{k}_i| = |\vec{k}_f| = 2\pi/\lambda$, and $\vec{r}_i$ is the position of the volume element dV in the sample reference frame. c) The Bragg condition.

with magnitude $|\vec{k}_f| = |\vec{k}_i| = 2\pi/\lambda$. The electronic density may change in time. This dynamics can be tracked by the time dependence of the structure factor.

In scattering theory, the first Born approximation [27] assumes weak scattering or a small scattering volume. This approximation is also used for the kinematic theory of X-ray diffraction. In this treatment, the Fraunhofer diffraction condition is assumed which means that the sample is illuminated by plane waves originating from a point source, placed far away from the scattering center. It is important to stress that in a typical scattering experiment, this condition is not fully satisfied and one must correct for the finite source size and input divergence (see Fig. 2.1a). For synchrotron radiation, this condition can be more easily satisfied because of the small input divergence and source size. In this thesis, the experimental setup is close to the Fraunhofer condition. This will change qualitatively the structure factor observed. We will discuss this in more detail in section 2.6.

For a crystal, the electronic density is periodic and has translational symmetry, so that

$$\rho(\vec{r}) = \rho(\vec{r} + \vec{T}), \quad \text{with } \vec{\mathrm{T}} = \mathrm{x}_1\vec{\mathrm{a}}_1 + \mathrm{x}_2\vec{\mathrm{a}}_2 + \mathrm{x}_3\vec{\mathrm{a}}_3, \tag{2.11}$$

where $\vec{T}$ is a translation vector obtained by a linear combination of the primitive translation vectors $\vec{a}_i$, and the integers x_i. The crystal electronic density is also periodic in Fourier space, with primitive translation vectors

$$\vec{G} = h\vec{b}_1 + k\vec{b}_2 + l\vec{b}_3, \text{ where} \tag{2.12}$$

$$\vec{b}_1 = 2\pi\frac{\vec{a}_2 \times \vec{a}_3}{\vec{a}_1 \cdot (\vec{a}_2 \times \vec{a}_3)}, \ \vec{b}_2 = 2\pi\frac{\vec{a}_3 \times \vec{a}_1}{\vec{a}_1 \cdot (\vec{a}_2 \times \vec{a}_3)}, \ \vec{b}_3 = 2\pi\frac{\vec{a}_1 \times \vec{a}_2}{\vec{a}_1 \cdot (\vec{a}_2 \times \vec{a}_3)}, \tag{2.13}$$

and h, k, l are integers called the Miller indices. Note that the vectors $\vec{a}$ and $\vec{b}$ are perpendicular, so $\vec{a}_i \cdot \vec{b}_j = 2\pi\delta_{ij}$, where $i, j = 1, 2, 3$. Using the fact that the Fourier transform of a crystal is also periodic in reciprocal space, it is easy to show[1] that scattering maxima occur in Eq. 2.10 when the scattering vector $\vec{q} \equiv \vec{G}$. These maxima are called Bragg peaks. The Bragg condition occurs when the phase difference between light scattered from parallel planes of atoms (see Fig. 2.1b) is a multiple of 2π. The scattering angle θ_B, shown in Fig 2.1c, is given by Bragg's formula

$$2d_{hkl}\sin\theta_B = \lambda, \tag{2.14}$$

where θ_B is the Bragg angle, and $d_{hkl} = 2\pi/|\vec{G}|$. For an infinite crystal, these Bragg peaks are Dirac delta functions in reciprocal space, but for a finite crystal of linear dimension D, their intrinsic width in reciprocal space is proportional to $1/D$. When some disorder with correlation length $\xi < D$ is present in the sample, the Bragg peak width becomes proportional to $1/\xi > 1/D$.

In a crystal, since the atomic positions are periodic, the structure factor $S(\vec{q})$ in Eq 2.10 can be rewritten as a sum of waves scattered by each lattice point in the crystal. Then, one finds

$$S(\vec{q}) \propto |\sum_i F\exp(-i\vec{q} \cdot \vec{r}_i)|^2, \tag{2.15}$$

[1] This is derived for example in Chap. 2 in Kittel [42].

where $\vec{r_i}$ are the positions of the lattice points in the scattering volume, and F is the form factor of all the atoms in the basis of the unit cell given by

$$F = \sum_j f_j \exp(-i\vec{q} \cdot \vec{r}_j), \tag{2.16}$$

where f_j and $\vec{r}_j$ are respectively the usual atomic form factor and position in the unit cell for the jth atom in the basis. Note that f_j is complex, with $f_j = f_{1j} + if_{2j}$[1]. For an orthorhombic lattice, it is easy to show [26], by evaluating the sums in Eq. 2.15, that the structure factor

$$S(\vec{q}) = |F|^2 \frac{\sin^2(N_1 a_1 q_x)}{\sin^2(q_x a_1)} \frac{\sin^2(N_2 a_2 q_y)}{\sin^2(q_y a_2)} \frac{\sin^2(N_3 a_3 q_z)}{\sin^2(q_z a_3)}, \tag{2.17}$$

where $\vec{q} = (q_x, q_y, q_z)$, and N_1a_1, N_2a_2, N_3a_3 are the sample linear dimensions. Fig. 2.7 shows the structure factor of a two dimensional square lattice with lattice constant a with 100×100 atoms. The peak intensity in this approximation is proportional to the square of the sample volume, the width of the Bragg peak along q_i is the inverse of the sample linear size $\Delta q_i \propto \frac{1}{N_i a_i}$, and the scattered integrated intensity over all wavevectors is proportional to the sample volume (or the total number of atoms). The side lobes in Fig. 2.7 are the secondary maxima of Eq. 2.17.

Another important property of scattered X-rays is the change of state of polarization of the incident beam by the scattering process. X-rays polarized perpendicular to the scattering plane, the plane parallel to both incident and scattered wavevectors, suffer no loss of intensity while those polarized in the scattering plane suffer a $\cos^2(2\theta_B)$ loss [26]. This effect can be used to make an X-ray polarizer or analyzer by scattering from a crystal with $2\theta_B = \pi/2$. In the experiments reported here, the scattering plane was vertical, and perpendicular to the polarization vector.

Finally, in X-ray scattering experiments, one needs to select a narrow energy band of the incident polychromatic beam. In the hard X-ray region of the spectrum, this is done by using Bragg reflection from a nearly perfect single crystal, called a monochromator. To understand the wavelength dependence of l_l, one needs to understand the

[1]The complex term is caused by absorption of the incident or scattered wave. For hard X-rays, $f_1 \approx Z$, where Z is the number of electrons in the atom and f_2 is related to the mass absorption coefficient, μ_m, by $f_2 = \mu_m \frac{A}{2N_A \lambda r_e}$[43], where A is the atomic mass, N_A the Avogadro number and $r_e = e^2/(4\pi\epsilon_0 m_0 c^2) = 2.82 \times 10^{-15}$ m the classical electron radius[41].

wavelength dependence of $\delta\lambda/\lambda$ for a single crystal monochromator. It is calculated by taking the derivative of Bragg's law in Eq. 2.14 with respect to λ. For a perfectly collimated polychromatic X-ray beam, it is easy to show [44] that the relative bandwidth

$$\delta\lambda/\lambda = \delta\theta/\tan\theta = r_e N\lambda^2 Re\{F\}/(\pi\sin 2\theta\tan\theta) \propto NRe\{F\}d_{hkl}^2. \tag{2.18}$$

Eq. 2.18 was simplified by replacing $\delta\theta$ by the Darwin width of an absorbing semi-infinite monochromator crystal with $\delta\theta = \frac{r_e N\lambda^2 Re\{F\}}{\pi\sin 2\theta}$ [26], where N is the electron density, r_e is the classical electron radius, $Re\{F\}$ is the real part of the form factor of the Bragg plane, and recalling that $\sin\theta = \lambda/2d_{hkl}$. One finds that $\delta\lambda/\lambda$ is weakly dependent on wavelength through the wavelength dependence of $Re\{F\}$. Brauer et al. [44] also consider the case where the incident X-ray beam has a finite divergence. Eq. 2.18 then becomes $\delta\lambda/\lambda = (\delta\theta + D_i)/\tan\theta$, where D_i is the input divergence. Then the relative bandwidth will be wavelength dependent through the wavelength dependence of θ.

2.4 X-ray scattering from Cu_3Au

The binary alloy Cu_3Au is a classical system for studying the properties of first order phase transitions. It has been studied for over half a century, and its equilibrium and non-equilibrium *incoherent* scattering is fairly well understood. Most of the earlier X-ray scattering work consisted of measuring the equilibrium properties of the alloy, like the equilibrium temperature dependence of the long range order, the anisotropy of the Bragg peak in reciprocal space due to the presence of antiphase domains, and the diffuse scattering from the short range order fluctuations. Several textbooks discuss the scattering from Cu_3Au [26, 27]. The focus of research on Cu_3Au has changed in recent years. For example, some of the work has been focused on studying the nature of the phase transition on the surface layers of Cu_3Au single crystals [45, 46, 47], while others have studied the non-equilibrium kinetics of Cu_3Au, after a quench from its disordered phase to the ordered phase [28, 29, 30, 31, 32, 33]. The latter work is motivated by a need to improve our understanding of non-equilibrium

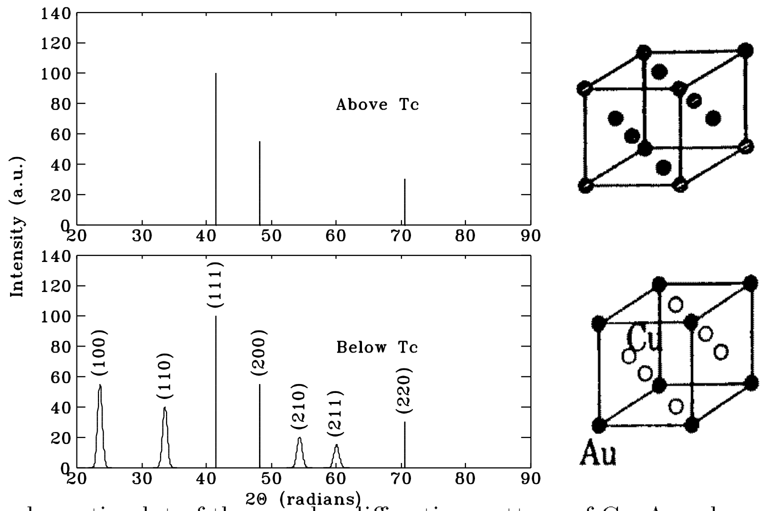

Figure 2.2: A schematic plot of the powder diffraction pattern of Cu_3Au, above and below T_c using $a = 3.771$ Å[32], and $\lambda = 1.5405$ Å, with domains below T_c of 100 Å. The equilibrium real space structure is shown beside. (From Ref. [27])

processes. These processes are important in the fabrication of many technologically relevant materials. Furthermore, since non-equilibrium processes are quite challenging conceptually, much work remains to be done to understand them.

Cu_3Au goes through an order-disorder transition at a critical temperature $T_c = 390°C$ [26]. Fig 2.2 shows the structure factor for a powder sample and the real space equilibrium structure above and below T_c. Below T_c, the structure is $L1_2$ with a basis consisting of one Au atom occupying the corner position $(0, 0, 0)$ of the cubic lattice with 3 Cu neighbors on the neighboring face center sites $(1/2, 1/2, 0)$, $(0, 1/2, 1/2)$, $(1/2, 0, 1/2)$ of the unit cell. Above this transition temperature, the structure is fcc because each atomic species diffuses through the lattice randomly, yielding an effective atomic form factor for each site of the basis given by $\overline{f} = 1/4 f_{Au} + 3/4 f_{Cu}$, where f_{Au} and f_{Cu} are the form factors of Au and Cu respectively. The peaks in Fig. 2.2 which remain unchanged above T_c are called fundamental peaks and are not affected by the degree of long range order in the crystal. The peaks that disappear above T_c are called superlattice peaks. Following Warren [26], it is easy to show that the integrated scattered intensity

$$S(h,k,l) = \begin{cases} 16(\frac{3f_{Cu}}{4} + \frac{f_{Au}}{4})^2 \text{ for } h,k,l \text{ all odd or even,} \\ \psi_{BW}^2 (f_{Au} - f_{Cu})^2, \text{ for mixed } h,k,l, \end{cases} \tag{2.19}$$

where ψ_{BW} is the Bragg Williams order parameter, ranging between zero in the disordered phase, to one in the fully ordered phase. The integrated intensity of a superlattice peak is proportional to the square of the order parameter, and to the square of the difference between the atomic form factors of Cu and Au. The fundamental peaks occur for unmixed h, k, l, and are independent of ψ_{BW}.

Although the long range order disappears above T_c, some weak scattering is still observable around the superlattice peak. It is due to the tendency of Au atoms, for example, to surround themselves with three Cu atoms as nearest neighbors, causing short range spatial correlations in the disordered states which are observable as diffuse scattering [27, 48].

The ordered state has a four fold degeneracy since the Au atom can occupy any of the four sites of the basic unit cell. This degeneracy leads to the formation of four competing phases forming large antiphase domains, separated by domain walls. There are two types of domain walls in Cu_3Au [30, 32]. Type I domains walls are formed by a half-diagonal glide in planes perpendicular to the cubic axes[1]. They have low interfacial energy because they do not require a change of nearest neighbor coordination along the interface [32]. Type II walls are formed by a half-diagonal glide across planes perpendicular to the cubic axes[2]. They have a higher interfacial energy because they require a change of nearest neighbor configuration. It is well known that these domain walls give rise to an anisotropy in the Bragg peaks of the ordered phase. Warren [26] derives the line shape of the superlattice peak, assuming that it is caused only by Type I walls, where domains forming along the three crystallographic axes are independent of each other, and the probability of crossing a domain wall, γ, is small. The scattered intensity for planes with Miller index (hkl), where h, k are indexes with the *same parity* is

$$S(hkl) = |F|^2 \frac{N_1 \gamma}{\gamma^2 + (\pi h)^2} \frac{N_2 \gamma}{\gamma^2 + (\pi k)^2} \frac{\sin^2(\pi N_3 l)}{(\pi l)^2}, \tag{2.20}$$

where the N_i are proportional to the sample linear size. This peculiar line shape gives

[1]In the [001] direction, this corresponds to displacing a domain with respect to another by 1/2[110]
[2]In the [001] direction,this corresponds to displacing a domain with respect to another by 1/2[101]

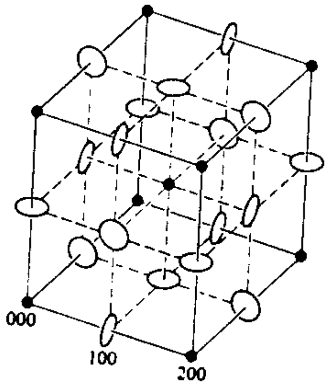

Figure 2.3: The superlattice peak in reciprocal space from Ref. [26]. It is anisotropic because Type I walls form in the three crystallographical direction. The fundamental reflections are shown with solid circles.

rise to disks in reciprocal space shown in Fig 2.3. For the (100) superlattice peak for example, this gives a disk oriented in a plane parallel to the (011), with the narrower dimension along the (100). A more detailed lineshape is given in Ref. [30].

Recent time-resolved studies of the ordering kinetics of Cu_3Au have revealed quite rich dynamical features of the ordering and coarsening process. Noda et al. [29] found that the structure factors in the later stage can be rescaled by a simultaneous renormalization of time and space, with the characteristic length $L(t) \propto t^{1/2}$. They found that a Lorentzian-square function was a good scaling function for all quench depths. They found evidence of an incubation time for the formation of a critical droplet size, which later grows to macroscopic size. This incubation time diverges as the temperature approaches the critical point.

Ludwig et al. [30] studied the early stage of the nucleation and growth process with a fraction of a second time resolution. They found evidence that the early kinetics of the short range order fluctuations for quench temperatures just below T_c is a relaxation to a metastable state, which then slowly decays by nucleation and growth. For lower temperatures, the time scales of the two processes become comparable, and for $T_c - T > 34$ K, they found evidence for continuous ordering at a temperature well above the classical spinodal temperature.

Nagler, Shannon et al. [31, 32, 33] identified three distinct kinematic regimes: nucleation, ordering and coarsening. A delay in the growth of the integrated intensity was attributed to an incubation time for nucleation like in Ref. [29]. It was found that the structure factor crosses over from having a Gaussian line shape during the early stage of the ordering process, where the ordered nuclei are small and embedded in a disordered matrix, to a Lorentzian-square line shape during the late time coarsening process. They found that the anisotropic disk shape reflection sharpens in time with the same exponents along the disk plane and through the disk axis. They showed that the scaling exponent in the coarsening regime is consistent with the non-conserved order parameter (NCOP) exponent $n = \frac{1}{2}$ for curvature driven growth.

We will study the late stage of the ordering kinetics of the phase transition after a quench from the high temperature fcc phase to the low temperature phase, and record the scattered intensity of the Cu_3Au (100) super-lattice peak with a CCD array (see Fig. 2.2).

2.5 Production of coherent X-rays: experimental method

Before the invention of lasers, incoherent thermal sources were used to produce coherent illumination. By collimating an incoherent source like a mercury arc lamp [49] with a small aperture, a coherent light source can be obtained. The first speckle patterns measured with hard X-rays were observed with an *incoherent* source! This was demonstrated by Sutton et al. [15] for an incoherent source of X-rays by limiting the beam size to dimensions comparable to its horizontal and vertical transverse coherent lengths, l_x, l_y, given by rewriting Eq. 2.2 as

$$l_x = \frac{\lambda R_s}{2d_{sx}},\ l_y = \frac{\lambda R_s}{2d_{sy}}, \tag{2.21}$$

where R_s is the distance between the source and the point of observation, while d_{sx} and d_{sy} are the horizontal and vertical source size. Fig. 2.4 shows a typical experimental set up for such an experiment. Common symbols are defined on page IX for convenience, and the particular experimental parameters for the two runs where we collected data are shown in Table 2.1. Typical values at wavelength $\lambda = 1.24$ Å are given in Table 2.2.

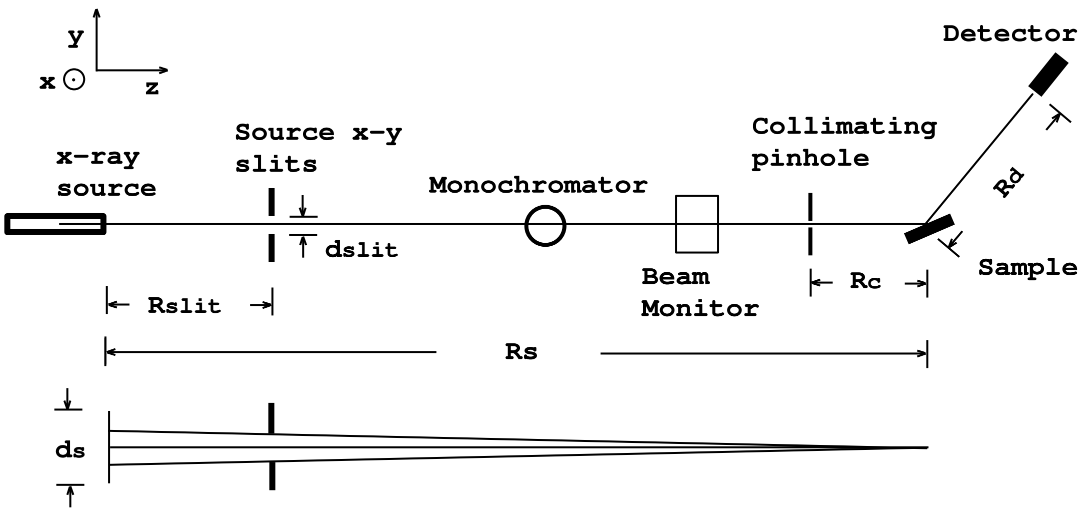

Figure 2.4: The experimental setup. All variables are defined on page IX for convenience, and their typical values are given in Table (2.1). The X-rays are generated by a wiggler or an undulator. The source x-y slits allow for a change of the coherence lengths by reducing the effective source size. A double Si (111) monochromator is set near 7.0 keV to prevent Cu fluorescence. The incident beam intensity is monitored by an ion chamber. The collimating pinhole is used to limit the beam size to a dimension comparable to the transverse coherence lengths. One of two detectors is normally used: a CCD array, or a scintillator masked by a micron size pinhole which is mounted on an x-y translation stage.

Table 2.1: Experimental parameters for the two experimental setups. The horizontal and vertical source sizes d_{sx} and d_{sy} are given by their full widths at half maximum (FWHM). The effective source size can be reduced by closing some upstream slits placed at a distance R_{slit} from the source.

Beamline	CHESS	NSLS X25
Source type	undulator	Wiggler
E keV	7.0	6.9
R_s m	25.8	27.8
R_{slit} m	17.8	10.5
d_{sx} mm	2.55	1.46
d_{sy} mm	0.167	0.068
R_c cm	6.7	6.75
R_d m	0.95	1.04

In a typical incoherent X-ray scattering experiment with a laboratory source, $\lambda = 1.54$ Å, $d_s \approx 1-10$mm, $R_s \approx 1$m resulting in $l_t \approx 80-800$ Å. Limiting the beam size to such small length scales would not give any useful coherent flux. Since the beam size at the sample position is also a few mm, the speckle pattern is washed out by incoherent averaging [10]. Because of the high collimation of third-generation X-ray sources and the large source-sample distances, typical coherence lengths are between 1-10 μm. Since these sources are several orders of magnitude brighter than conventional sources, one can obtain a coherent beam with sufficient flux by collimating the incident beam with pinholes of diameter comparable to $l_{x,y}$ (typically $4-7\mu$m).

The coherent flux, Φ_c, is calculated from the integrated flux going through a rectangular aperture with height l_y and length l_x, which accepts the full source divergence α_x, α_y. It is easy to show that

$$\Phi_c = \frac{\lambda^2 B(\lambda)}{4}\frac{\delta\lambda}{\lambda}, \tag{2.22}$$

where $B(\lambda)$ is the brightness of the source. The relative bandwidth $\delta\lambda/\lambda$ selected by the monochromator is only weakly dependent on wavelength as shown in Eq. 2.18. Therefore the presence of the λ^2 term makes these experiments easier to perform at longer wavelengths. Typical values of this flux at X25 and CHESS are given in Table 2.2. With 1.2×10^6 photons/s, X25 gives a coherent flux comparable to a laboratory source. An increase of a factor 500 should be gained by performing experiments at the Advanced Photon Source (APS).

Past and current coherent X-ray experiments can be limited by this small coherent

Beamline	l_t μm	l_l μm	B	Φ ph/s
X25 NSLS	1-25	0.44	3×10^{14}	1.2×10^6
CHESS Undulator	0.6-10	0.44	3×10^{15}	1.2×10^7
APS Undulator	10-10	0.44	1.5×10^{17}	6×10^8

Table 2.2: Brightness and coherence lengths for different sources at 1.24 Å. Brightness measured in $ph/s/mm^2/mrad^2/0.01\%BW$.

flux. A currently active area of research is investigating ways to improve the flux going through the collimating pinhole, by sacrificing some vertical coherence with focusing X-ray optics like a mirror [50, 51] or asymmetrically-cut crystals [44, 52]. The idea originated from the fact that l_y is typically an order of magnitude larger than l_x for synchrotron radiation, so that if one focuses the X-ray beam in the vertical direction until the vertical divergence matches the horizontal divergence, then $l_y = l_x$, and the coherent flux is increased through the pinhole because of the focusing. These techniques are important since they will make it possible to tailor the coherence volume $l_x l_y l_z$ for a given experiment requiring, for example, a much smaller beam size than the smallest of the transverse coherence lengths, or requiring equal horizontal and vertical transverse coherence lengths [44].

Another approach for improving the scattered intensity is by optimization of the product of the coherent flux, Φ_c, and the fraction of scattered X-rays with respect to energy. One can show[1] that the integrated scattered intensity for Cu_3Au

$$I_s \approx B(\lambda)\lambda^2 \frac{\delta\lambda}{\lambda}\psi^2 \mu_{Cu_3Au}|f_{Au} - f_{Cu}|^2, \tag{2.23}$$

where ψ is the order parameter, f_{Cu} is the complex atomic form factor for Cu, and μ_{Cu_3Au} is the absorption length in Cu_3Au. Eq. 2.23 depends on the X-ray contrast of the two elements Cu and Au. One way to increase the scattered intensity for the study of order-disorder transitions is to choose the material with the largest difference in atomic number. For the sake of simplicity, let us assume a fully ordered material, with $\psi = 1$, and assume that one can tune the insertion device in such a way that B is constant over the wavelength range of interest. Fig. 2.5 shows the approximate scattered intensity integrated in q over the (100). The energy in this experiment was set to 7 KeV, which is close to the optimal condition for Cu_3Au. In a real experiment, windows and monochromators may complicate this relationship; thus, it is often simpler to measure the scattered intensity in order to optimize it.

[1] One needs to combine absorption effects and the integrated intensity of a superlattice peak in a binary alloy found in Eq. 2.19, assuming no polarization losses.

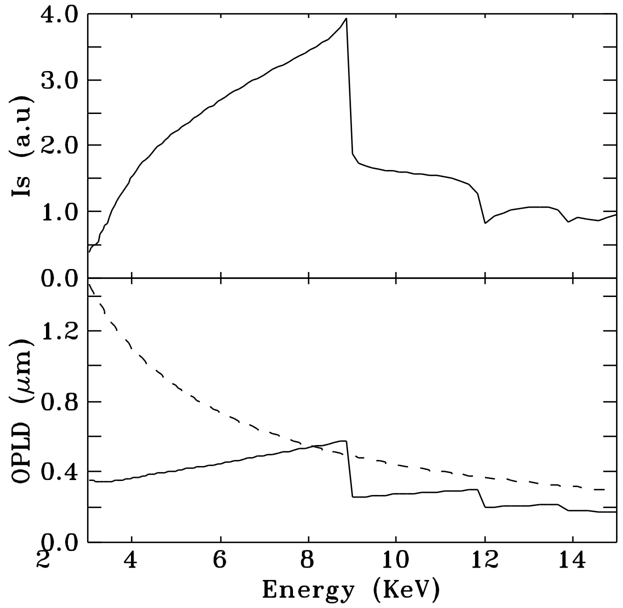

Figure 2.5: The energy dependence of the scattered intensity I_s calculated from Eq. 2.23. The atomic form factors for Cu and Au were taken from Ref. [53], and the mass absorption coefficients were calculated from these form factors. The discontinuities are the absorption edges for Cu (near 9 keV) and Au (near 12 and 13.7 keV). Below, the optical path length difference in Cu_3Au $2\mu \sin^2 \theta_B$ (solid line) and the longitudinal coherence length l_l (dashed line). Here l_l is calculated from Eq. 2.1 and 2.18, neglecting the weak energy dependence of $Re\{F\}$ for the Si (111) monochromator (only 1.5 % change over the energy range shown).

2.5.1 Coherence volume

The other condition for coherent scattering is that the optical path length differences (OPLD) in the sample be smaller than the longitudinal coherence length of the source, l_z, such that

$$OPLD < l_z = \frac{\lambda^2}{2\delta\lambda}, \tag{2.24}$$

where $\delta\lambda/\lambda$ is the relative wavelength bandwidth of the source of radiation [38]. For 7.0 keV X-rays, filtered with a Si_{111} monochromator, $\delta\lambda/\lambda = 1.4 \times 10^{-4}$, giving $l_z \approx 0.6\ \mu$m. This coherence condition is achieved by using a thin sample, or a sample with large enough absorption, or by scattering with a grazing angle of incidence [16, 17]. Specialized monochromators can also be used to change the longitudinal coherence length. For example, Dierker et al. [22] have used a wide bandpass X-ray multilayer monochromator to select the smallest l_l possible in order to maximize the available coherent flux. It is also possible to increase l_l by using higher order reflections of Si, or by using high resolution monochromators like those used for

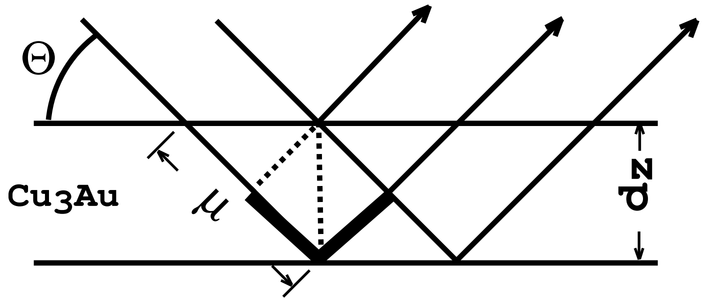

Figure 2.6: The condition for longitudinal coherence. It is satisfied because the optical path difference (wider line), $2d_z \sin\theta$, is smaller than the longitudinal coherence length. The X-ray penetration depth perpendicular to the surface is $d_z = \mu \sin\theta$, where μ is the sample X-ray absorption length. Therefore, the longitudinal coherence condition is rewritten as $l_l < 2\mu \sin^2\theta$.

Mössbauer scattering or high energy inelastic scattering [54].

For Cu_3Au, the absorption length at 1.77 Å is $\mu = 4.2$ μm [55]. The difference in optical path is illustrated in Fig. 2.6 for a symmetric Bragg reflection. The Bragg angle $\theta = 13.67°$, and d_z is the X-ray penetration depth in the material perpendicular to the surface. The longitudinal coherence condition is fulfilled because the path length difference, $2d_z \sin\theta = 2\mu \sin^2\theta = 0.47\mu$m, is smaller than l_z. Note also that for Cu_3Au, the OPLD is smaller than l_l for all energies below 8.1 KeV or above 9.0 KeV as seen in Fig. 2.5.

The longitudinal coherence condition depends on the angle θ of the reflection. Pindak et al. [18] have clearly demonstrated this effect by observing the contrast of speckle patterns on superlattice reflections of a charge density wave in $K_{0.3}MoO_3$. For this material, the longitudinal coherence condition is valid for $\theta < 9.5°$ [18]. They demonstrated that speckle is observable for low order reflection with $\theta < 11°$, but disappears for reflections with $\theta = 22.5°$.

2.6 Structure factor with coherent X-rays

Here two models are presented which give the reader a few examples on the present and possible uses of coherent X-ray beams.

2.6.1 Coherent X-ray scattering for the study of isolated defects or artificially made structures

It is important to realize that the definition of the structure factor must be slightly modified to take into account the coherence of the beam. The measured structure factor is typically an *ensemble average* of the coherent structure factor calculated over the coherence volume of the source. This ensemble average is typically performed over the illuminated volume $V >> l_x l_y l_z$, where the coherence volume is the product of the coherence lengths. Mathematically formulated, the structure factor observed in a typical X-ray experiment is

$$S(\vec{q},t) = <| \int_{l_x l_y l_z} d\vec{r} \rho(\vec{r}) e^{-i\vec{q}\cdot\vec{r}_i} |^2>_V. \tag{2.25}$$

When the illuminated volume is comparable to the coherence lengths of the source, the structure factor becomes sensitive to individual realizations of the ensemble, thus becoming sensitive to the exact position of the atoms in the illuminated volume.

The first *theoretical* model shown here was suggested in the original demonstration of speckle by Sutton et al. [15]. It consists of isolating single defects in a few μm diameter beam to study the detailed microstructure of the material and to improve our structural understanding of defects in condensed matter. In typical X-ray experiments, one illuminates millions of defects *incoherently*, since the illuminated area is typically 1 mm$\times$1 mm but the X-ray beam transverse coherence lengths are on the order of 1000 Å. Since the characteristic length scale of a defect ranges between a few Å to a few μm, the presence of defects is seen only in slight changes of the line shape of the Bragg peak which can be hard to interpret as a given defect type.

As opposed to incoherent experiments, coherent X-ray scattering techniques are more sensitive to the exact position of atoms in the scattering volume. It gives a structure factor that is very different depending on the type of defects illuminated. An example of this sensitivity to disorder is shown in Fig. 2.7. The structure factor of a two dimensional perfect crystal with a square lattice calculated using Eq. 2.17 is shown. The calculation is shown for a crystal of 100×100 atoms. The peak height

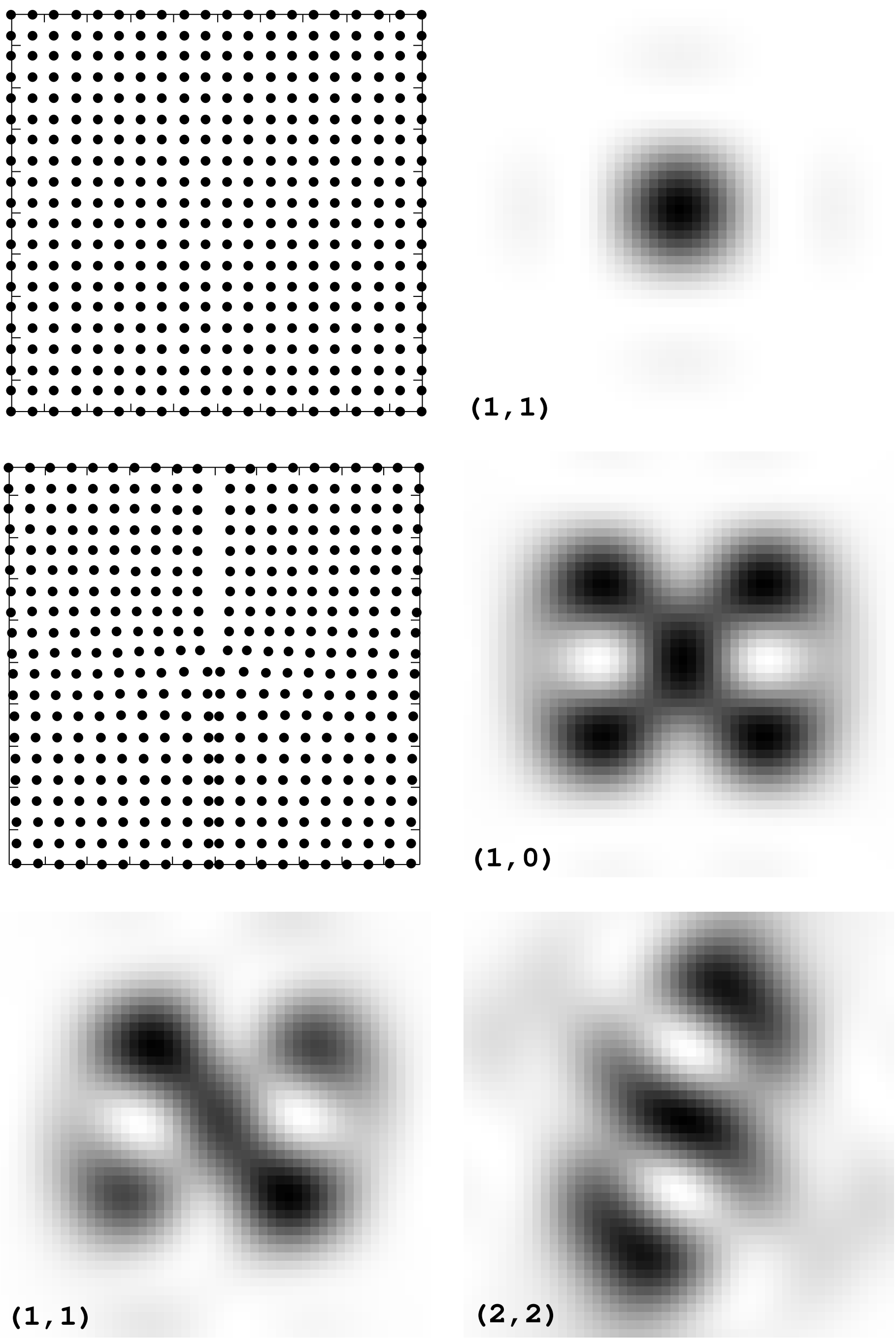

Figure 2.7: (Top left) The central 20×20 atoms in a real space square lattice with lattice parameter a, and $S(\vec{q})$ centered on the (1,1) (top right). A linear grey scale from 0 to 10^8 is used to display the (1,1). The wave vector range shown from the $(1,1)$ centered on the middle of the image is $(2\pi/a \pm 4\pi/L, 2\pi/a \pm 4\pi/L)$, where the sample size $L = 100a$. (Middle) The central 20×20 atoms of a real space two dimensional lattice distorted by an edge dislocation, and $S(\vec{q})$ centered around the $(1,0)$ using the same range as the top image. (Bottom) $S(\vec{q})$ centered around the (1,1) and (2,2). The Bragg peaks split into several satellites. The structure factor varies depending on the position in reciprocal space.

goes as the square of the number of atoms, and its width as the inverse of the sample size. The middle image in Fig. 2.7 shows the real space lattice of a crystal distorted by an edge dislocation[1]. The structure factor calculated from Eq. 2.15 is also shown for the (1,0), (1,1) and (2,2). The original structure factor of the perfect lattice is split into satellites of comparable magnitude but weaker intensity than the perfect crystal. The splitting of the satellites is on the order of the FWHM of the perfect square lattice. In order to look at defects on a quasi-perfect single crystal of Si, one would look for structure on an angular scale comparable to the Darwin width of Si. By using a high resolution set up, this experiment could be feasible.

One should note that some experiments have already been done on simple structures, such as two-dimensional gratings and multilayers. Recently, Robinson et al. [17] observed speckle from a multilayer of $GaAs_xAlGaAs_{1-x}$. They developed several theoretical approaches which could fit the observed random speckles. They found that coherent X-ray scattering can be quite a sensitive tool for studying the disorder of the lattice orientation on the surface of their multilayers. It appears that it can give additional information which cannot be obtained from other experimental techniques.

Shen et al. [57] studied the structure of a two dimensional grating, using X-rays with a transverse coherence length of the order of one μm. They did not match the illuminated volume with the transverse coherence length of the source, thus some ensemble average was performed. The measured X-ray scattering was modeled adequately with the kinematic theory using a sample size given by the transverse coherence length of the source. They found that the added transverse coherence gives microscopic as well as additional mesoscopic information on the grating structure, such as its period, width and shape, atomic registry with the substrate, and crystal lattice strain. Recently, Tanaka et al. [58] have used the technique demonstrated above to measure surface diffusion and strain in the same oxidized grating as in

[1]The displacements $d\vec{r} = (dx, dy)$ for all atoms were calculated by a simple model of an edge dislocation, given by Eq. 30.6 in Christian [56]. Here the displacement of the atom at position $\vec{r} = (x, y)$ in the crystal is $dx = b/4\pi(1-\nu)[2(1-\nu)\arctan(y/x) + xy/(x^2+y^2)]$, and $dy = -b/4\pi(1-\nu)[(1-2\nu)\ln(x^2+y^2) - x^2/(x^2+y^2)]$, using a Poisson Ratio $\nu = 1/3$, and a Burgers vector $b = a$, where a is the lattice parameter.

Ref. [57].

2.6.2 Scattering from a binary alloy in equilibrium

We derive next some of the properties of the structure factor $S(\vec{q},t)$ obtained with coherent light incident on a typical binary alloy like Cu_3Au and Fe_3Al, in thermal equilibrium below the critical temperature, T_c, of a first order or a continuous phase transition. This section is motivated by the need to understand the equilibrium short range order fluctuations in equilibrium and non-equilibrium experiments which occur within large antiphase domains. This section serves also as a good demonstration of equilibrium IFS. The results derived below are valid for a large class of systems like magnetic systems and binary alloys belonging to the non-conserved Ising universality class. The discussion is limited to the region well above or well below a continuous phase transition, outside the critical region[1]. The properties of the $S(\vec{q},t)$ for a system in the conserved Ising universality class will be qualitatively consistent with those of the non-conserved order parameter, although the exact dynamical properties will have a different wavevector dependence due to the conservation laws.

The *theoretical model* used for this demonstration is a time-dependent Landau-Ginzburg field theory model called model A in the Hohenberg and Halperin classification scheme [59]. This model describes well the equilibrium and non-equilibrium properties of a binary alloy with a non-conserved order parameter [60, 61], where the order parameter is proportional to the sublattice concentration of one of the atomic species. The equilibrium dynamics of the order parameter is obtained by minimizing a coarse-grained free energy F and solving

$$\frac{\delta\psi(\vec{r},t)}{\delta t} = -M\frac{\delta F}{\delta\psi} + \eta(\vec{r},t), \tag{2.26}$$

where $\psi(\vec{r},t)$ is the order parameter measured at discrete position $\vec{r}$ on a square lattice and at discrete time t, M is the mobility, and $\eta(\vec{r},t)$ is a noise term which takes into account the coupling of the system to the thermal bath by fast variables. Here, the

[1] For a review of critical dynamics, see Hohenberg and Halperin [59].

noise term is Gaussian and uncorrelated in space and time with

$$<\eta(\vec{r},t)\eta(\vec{r'},t')> = 2k_B T M \delta(\vec{r}-\vec{r'})\delta(t-t'), \text{ and } <\eta(\vec{r},t)> = 0, \tag{2.27}$$

where k_B is the Boltzmann constant, $\delta(x)$ is the Dirac delta function, and the brackets refer to an ensemble average. The free energy functional used is

$$F = \int d\vec{r} \left(\frac{\kappa}{2} |\nabla\psi(\vec{r},t)|^2 + \frac{r}{2}\psi^2(\vec{r},t) + \frac{w}{4}\psi^4(\vec{r},t) \right), \tag{2.28}$$

where κ, r, and w are phenomenological constants, with $w > 0$, and $r = r_0(T/T_c - 1)$, such that $r > 0$ in the disordered phase above T_c, and $r < 0$ when two ordered phases are stable below T_c, and $r = 0$ at T_c. The gradient term is used to model the interfacial free energy between two different phases. In the single phase equilibrium above T_c, F has a single well centered at the equilibrium value $<\psi> = 0$. Below T_c, F has a double well, with symmetric minima at $\psi = \pm\sqrt{\frac{-r}{w}}$.

Eq. 2.26 can be rewritten as

$$\frac{\delta\psi(\vec{r},t)}{\delta t} = -M \left(r\psi(\vec{r},t) + w\psi^3(\vec{r},t) - \kappa\nabla^2\psi(\vec{r},t) \right) + \eta(\vec{r},t). \tag{2.29}$$

Eq. 2.29 was solved numerically using Euler's method to discretize time and a nearest-neighbor approximation was used for ∇^2 [60]. The simulations were performed in two dimensions using periodic boundary conditions, and system sizes of 128^2, 256^2, or 512^2. For this simulation, the thermodynamic constants were set to one such that $\kappa = -r = w = M = 1$. To simulate the equilibrium dynamics, one of the phases was selected by setting the initial condition $\psi = \sqrt{\frac{-r}{w}}$, after which ψ was updated until the system reached equilibrium. After reaching equilibrium, the structure factor was simulated with time steps ranging between $dt = 0.005 - 0.05$.

To understand the static and dynamic properties of the equilibrium order parameter, let us study the disordered state. Above T_c, one can neglect the cubic non-linear term in Eq. 2.29. Then, the dynamics of the order parameter is given by a stochastic linear equation, which can be easily solved. Taking the Fourier transform of Eq. 2.29, on finds

$$\frac{\delta\psi(\vec{q},t)}{\delta t} = -M(r+\kappa q^2)\psi(\vec{q},t) + \eta(\vec{q},t). \tag{2.30}$$

From this equation, one sees clearly that large time fluctuations of the order parameter will be exponentially damped with correlation time

$$\tau_c = \frac{1}{M(r+\kappa q^2)}. \tag{2.31}$$

Long wavelength fluctuations of the order parameter have slower decay rates than shorter wavelength fluctuations. This will be important for understanding the time correlation of the structure factor discussed later. Below T_c, a similar treatment can be done by a Taylor expansion of ψ in Eq. 2.29 around its equilibrium value $\psi = \pm\sqrt{-r/w}$. Then one finds $\tau_c = \frac{1/M}{\kappa q^2 - 2r}$. Note that for a conserved order parameter, the long range diffusion yields an extra q^2 dependence in the denominator, thus τ_c diverges at low $\vec{q}$ [12].

Following Eq. 2.10, the structure factor $S(\vec{q},t) = \psi(\vec{q},t)\psi^*(\vec{q},t)$, where $\psi(\vec{q},t)$ is the Fourier transform of the order parameter. The *time independent* ensemble averaged structure factor is the well known Ornstein-Zernicke structure factor given by

$$S(\vec{q}) = \begin{cases} \frac{I_{SR}}{r+\kappa q^2} \text{ for T} > \text{T}_c, \\ I_{LR}\delta(\vec{q}) + \frac{I_{sr}}{\kappa q^2 - 2r} \text{ for T} < \text{T}_c, \end{cases} \tag{2.32}$$

where I_{LR} and I_{SR} are respectively the peak intensities of the long range order and short range order.

Note that to obtain Eq. 2.32, an ensemble average over *all possible configurations* was done. If one looks at the structure factor of the instantaneous atomic configuration $S(\vec{q},t)$, one does not simply observe a Lorentzian. Fig 2.8 shows $S(\vec{q},t)$ for a typical binary alloy in equilibrium below T_c, numerically simulated with model A. Regions with large intensity are next to regions with low intensity, with a characteristic size of one pixel in the image, corresponding to

$$\Delta q = 2\pi/L, \tag{2.33}$$

where L is the sample linear dimension. The equilibrium fluctuations of the scalar order parameter add a random modulation to the ensemble averaged structure factor in Eq. 2.32. A slice through the structure factor is shown next in Fig 2.9 for $q_y = 0$.

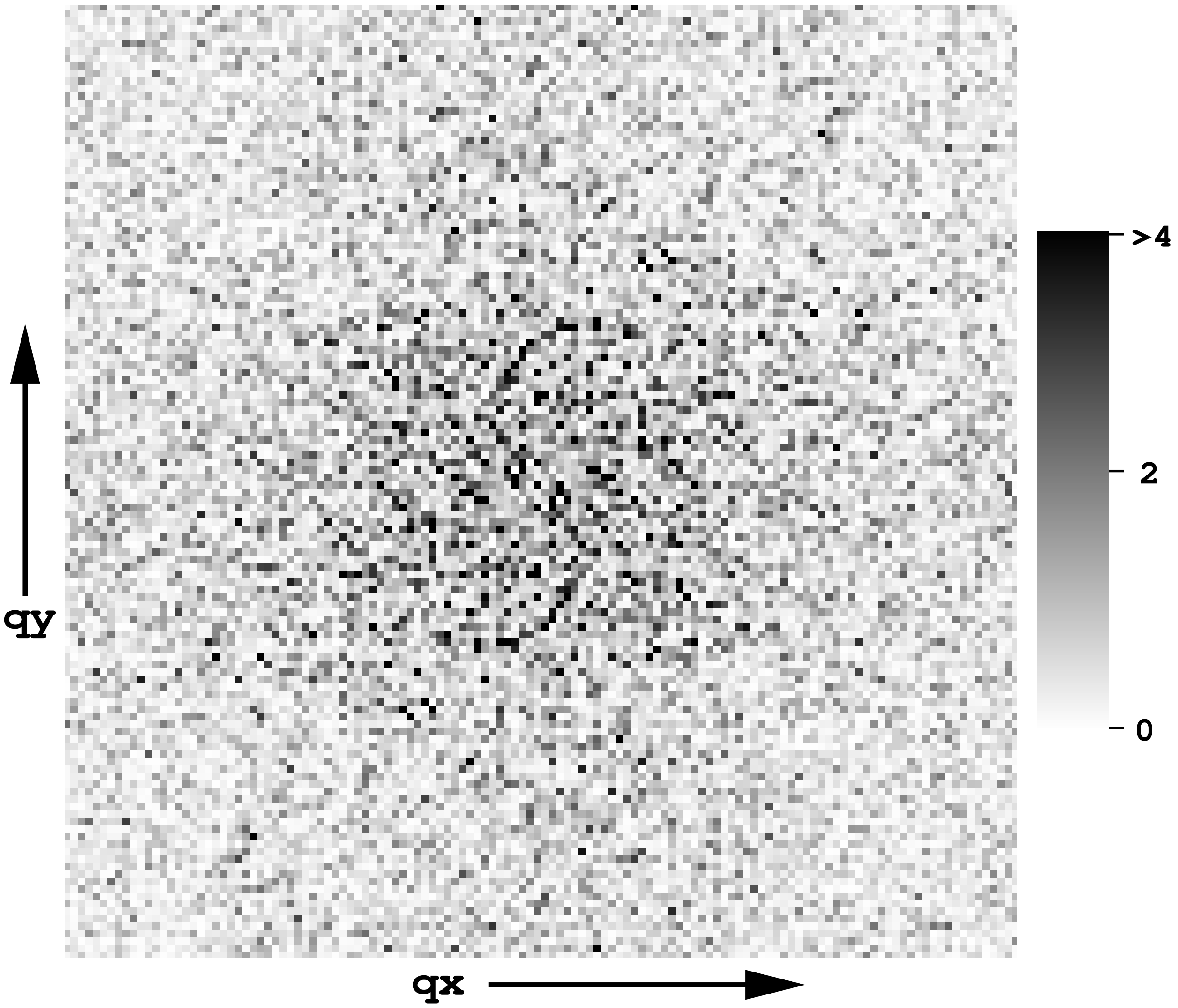

Figure 2.8: The instantaneous structure factor $S(\vec{q},t)$ for a typical binary alloy below T_c for a given time t. A linear grey scale between 0 and 4 is used to display $S(\vec{q},t)$. A slice through the origin of reciprocal space is shown in Fig. 2.9. The large spatial fluctuations with a characteristic length of 1 pixel are speckles, caused by the short range order equilibrium fluctuations. In a typical incoherent scattering experiment, the large spatial fluctuations disappear, and one observes that $S(\vec{q})$ is a smoothly varying function of $\vec{q}$, independent of the exact atomic arrangement. The coherent illumination allows one to measure the time fluctuations of the structure factor in equilibrium by studying the time fluctuations of the speckle pattern.

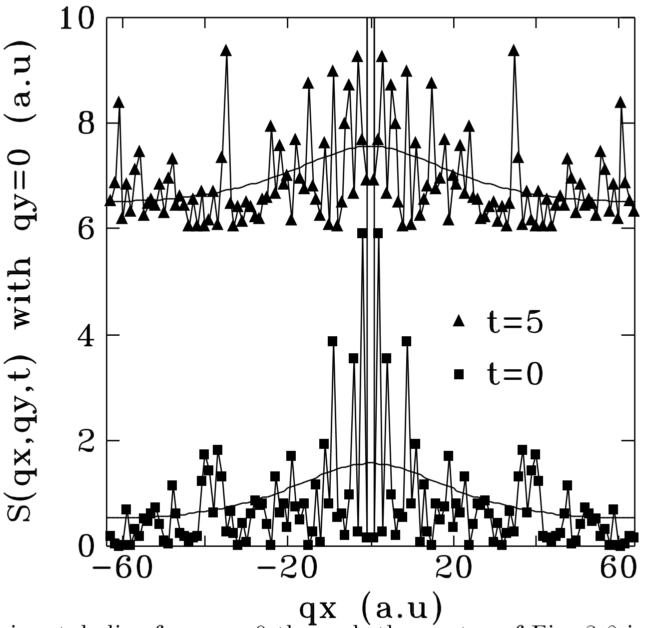

Figure 2.9: An horizontal slice for $q_y = 0$ through the center of Fig. 2.8 is shown with squares. The ensemble averaged structure factor defined in Eq. 2.32, observed in a typical incoherent experiment, is shown for comparison. The Bragg peak corresponding to the long range order is not seen because it is four orders of magnitude larger than the short range order diffuse peak. The structure factor at a later time $t = 5$ is also shown with triangles. A constant of 6 was added to the second slice for clarity. The speckle patterns shown differ because they depend on the exact arrangement of the atoms in the scattering volume which changes in time.

Note the large contrast in the structure factor. The most probable value is zero! The spatial fluctuations of $S(\vec{q},t)$ are as large as the ensemble averaged structure factor shown with a smooth solid line.

Fig. 2.8 and 2.9 show that the structure factor of a material with a random atomic configuration is also *random*! It is a well known property of the structure factor[1] in Eq. 2.10. For many people, this may come as a surprise, but this is observed regularly in light scattering experiments, and was first observed more than a century ago in the light scattering from small particles [3, 4, 5]! This effect is the same one that causes laser speckle from reflected or transmitted light on the rough surfaces of optical elements [6]. It is not observed in standard X-ray or neutron scattering experiments because the beam is incoherent. In general, the speckle contrast is lost because the sample is illuminated by many coherence volumes, or because the detector

[1] For example, on page 552 of Numerical Recipes [62], it is shown that the standard deviation of the power spectrum is equal to its average. Since the structure factor is the power spectrum for spatial fluctuations, the fluctuations in the structure factor are as large as their average! Crystallographer have also derived an exponential probability distribution of $S(\vec{q})$ for random reciprocal vectors [63].

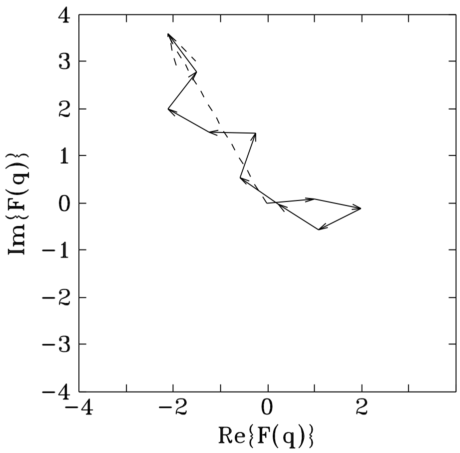

Figure 2.10: The complex scattering amplitude $F(\vec{q}) = \sum_i f_i e^{-\vec{q}\cdot\vec{r}_i}$ for ten atoms for a given $\vec{q}$, based on Fig. 4.2 in Ref [39]. As the number of atoms goes to infinity, the real and imaginary parts of $F(\vec{q})$ become independent Gaussian random variables. The dashed line is the resulting scattering amplitude, and the square of its magnitude is the structure factor $S(\vec{q})$.

resolution is insufficient to see the phenomena.

A speckle pattern is caused by coherent diffraction from random inhomogeneities in the material adding constructively or destructively, yielding a random structure factor. The speckle pattern is associated with the exact spatial arrangement of atoms in the scattering volume. This makes the structure factor sensitive to the individual realizations of a given statistical ensemble of atomic arrangements. This sensitivity is shown clearly in Fig. 2.9 since the speckle pattern for time $t = 0$ completely differs from the speckle pattern at later time $t = 5$.

Note also that if the crystal is perfectly ordered, the scattering is narrow and strong but only one speckle is observed. If the scattering is broad, many speckles are observed but the intensity of each speckle is small. For example, Fig. 2.9 is a sum of a narrow and broad component. The Bragg peak at $\vec{q} = 0$ subtends only one speckle. The scattering from the short range order fluctuations subtends many speckles, but its structure factor is four orders of magnitude smaller than the Bragg peak.

A speckle pattern is characterized by large spatial fluctuations from the ensemble average. This property follows from the definition of the structure factor in Eq. 2.15. We can represent Eq. 2.15 as a sum of random vectors in the complex plane. This is shown in Fig. 2.10 using ten atoms. Assuming that the phase factor $\vec{q} \cdot \vec{r}_i$ samples uniformly a range of phase difference from 0 to 2π, one can show [64], by invoking the central limit theorem, that the real and imaginary part of the complex scattering amplitude are *independent* Gaussian random variables. Since $S(\vec{q})$ is the sum of the squares of the real and imaginary scattering amplitudes, which are two independent Gaussian random variables, it can be shown[1] that $\rho(S)$ follows a negative exponential probability distribution

$$\rho(S(\vec{q})) = \frac{\exp(-S/\overline{S(\vec{q})})}{\overline{S(\vec{q})}}. \tag{2.34}$$

This distribution has a large *contrast*[2] defined as the ratio of its rms fluctuations over its average, $\sigma_S/\overline{S} = 1$.

By observing the structure factor at a given wavevector, one can measure the equilibrium fluctuations of the alloy. This is shown in Fig 2.11(a). Note the large fluctuations of the structure factor as a function of time. The amplitudes of the time fluctuations are as large as the average scattering. The structure factor fluctuates in time with a characteristic time scale which can be determined by the time correlation function of the time dependent structure factor. By calculating the time correlation function of $S(\vec{q}, t)$,

$$g_2(\vec{q}, \tau) - 1 = \frac{<S(\vec{q}, t)S(\vec{q}, t+\tau)>_t - <S(\vec{q}, t)>_t^2}{<S(\vec{q}, t)>_t^2}, \tag{2.35}$$

we can measure the characteristic time of the fluctuations.

Fig 2.11(b) shows g_2 for four given wavevectors. The time correlation function decays faster for larger $|\vec{q}|$, because short length scale fluctuations are intrinsically faster than long length scale fluctuations. The correlation functions shown in Fig. 2.11(b) were fitted to exponential decays $g_2(\tau)-1 = \exp(-\tau/\tau_c)$. The inverse of the fitted correlation time is shown in Fig. 2.11(c), where $1/\tau_c = 4+2q^2$. One expects the structure factor fluctuations to decay with $1/\tau_c = M(2q^2-4r)$ below T_c, and $1/\tau_c = M(2q^2+2r)$ above T_c. The factor two comes from the fact that we are measuring intensity fluctuations and not amplitude fluctuations[3]. This is the expected result for light with a

[1] See section A.1 for more details on the probability distribution of speckle.

[2] See for example section 4.2 in Goodman [39] or section 5.9 in Frieden [64].

[3] This factor of two is present in *homodyne* scattering. Homodyne refers to a scattering condition where the scattered beam interferes with itself. See Ref. [12], page 60 for more detail.

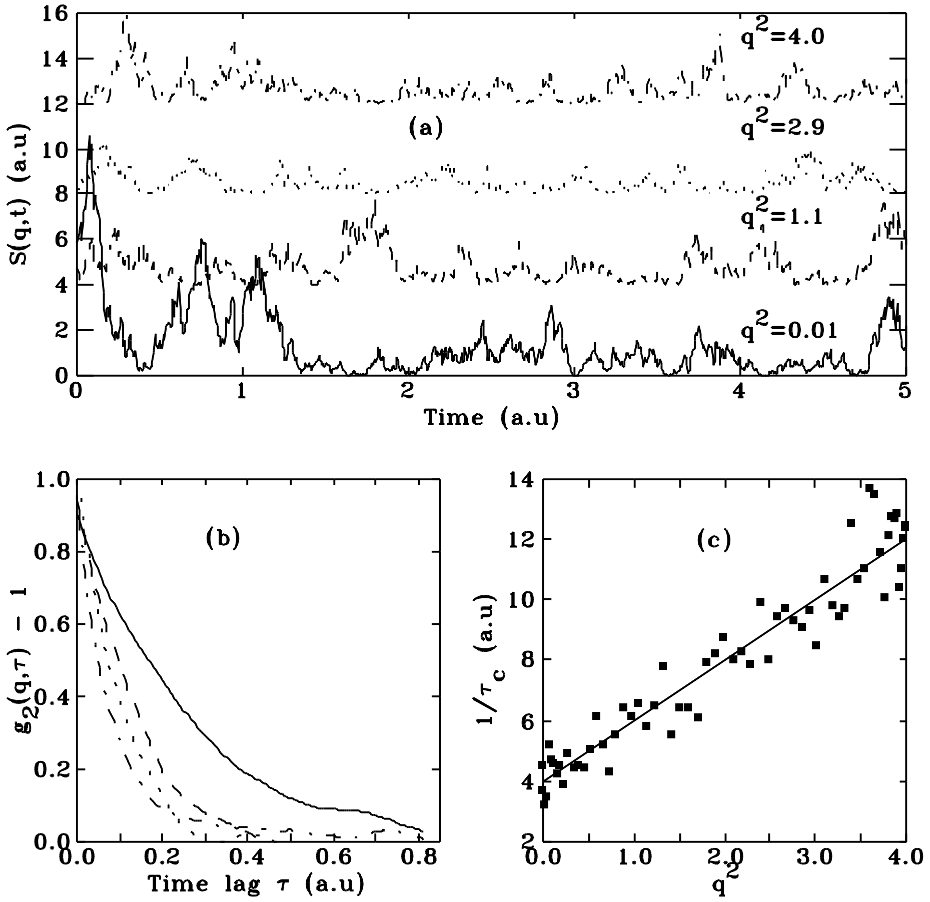

Figure 2.11: (a) The time fluctuation of the equilibrium structure factor displayed for four different wavevectors. The simulation was performed with the thermodynamic constants $\kappa = -r = w = M = 1$. In order to distinguish each wavevector, a constant (4,8,12) was added to the slices at increasing wavevectors. In an incoherent experiment, only the ensemble average is observed, thus the structure factor is constant in time. With coherent illumination, the structure factor at the four chosen wavevectors fluctuates in time with a characteristic time τ_c, which can be measured by a time correlation function defined in the text, and shown in (b). The characteristic time for the smallest wavevector (solid line) is 0.255, while it is 0.07 for the largest wavevector (dot-dashed line). The early decay of g_2 was fitted to $g_2(\tau) - 1 = \exp(-\tau/\tau_c)$. (c) The inverse of the least-squares fit correlation time $1/\tau_c$ versus q^2. As discussed in the text, it clearly fits $4 + 2q^2$.

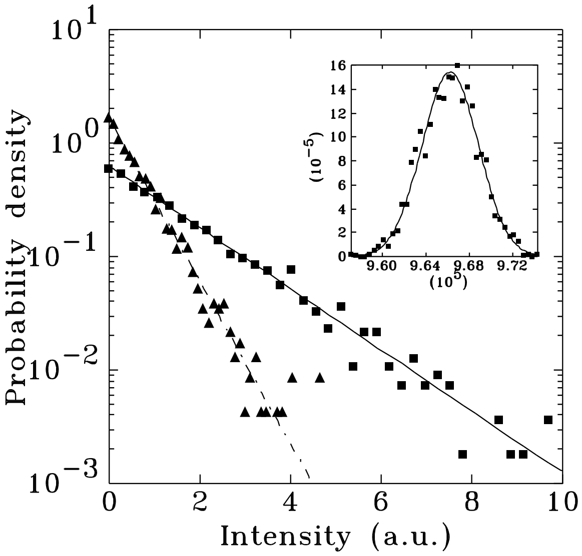

Figure 2.12: The probability density of the scattered intensity $S(\vec{q})$ for a binary alloy in equilibrium below T_c. $S(\vec{q})$ was simulated with model A. The squares and triangles are respectively the probability density of $S(\vec{q})$ for the smallest and largest $\vec{q}$ in Fig 2.11. The simulation results are in perfect agreement with the exponential distributions drawn with solid and dot-dashed lines, discussed in the text. An exponential distribution implies that $S(\vec{q})$ is non-self-averaging. The inset shows that the probability density of $S(\vec{q}=0)$ is nearly Gaussian, showing the scattered intensity self-averages for $\vec{q}=0$.

Lorentzian spectrum. Here $r=-1$, $M=1$, $\kappa=1$, in agreement with the fits. For systems with a conserved order parameter where the intensity fluctuations are caused by diffusion, the inverse of the correlation time $1/\tau_c = 2q^2 M(r+\kappa q^2)$ above T_c. The extra q^2 dependence comes from the added conservation law.

Fig 2.12 shows the equilibrium probability density of the scattered intensity, $\rho(S)$, calculated for model A below T_c. The probability density of $S(\vec{q})$ for two wavevectors is shown. The solid lines are $\rho(S) = \frac{\exp(-S/<S>)}{<S>}$, where $\rho(S)$ and the ensemble average of the equilibrium intensity, $<S>$, are calculated over 2^{14} independent measurements of $S(\vec{q},t)$, separated from each other by several correlation times. As discussed above, the scattered intensity in equilibrium is non-self-averaging[1] for $\vec{q} \neq 0$. Note that although the order parameter in equilibrium is self-averaging [65], the scattered intensity is not.

As shown in the inset of Fig 2.12, the probability density of $S(\vec{q}=0)$ is well

[1]A thermodynamic variable whose relative fluctuations vanish in the thermodynamic limit is called self-averaging. Here the time fluctuations of $S(q,t)$ are as large as the time average of $S(\vec{q})$ even in the thermodynamic limit.

fitted to a Gaussian, with $\rho(S) = \frac{\exp(-0.5(S-<S>)^2/\sigma_S^2)}{\sqrt{2\pi\sigma_S^2}}$, where the standard deviation of the scattered intensity $\sigma_S = 2583$, and the average intensity $<S> = 96622$ is calculated from the data. Recall that $S(\vec{q} = 0) = (\int \psi(\vec{r})d\vec{r})^2 = M^2$, where M is the magnetization of the system. The magnetization is an extensive quantity that self-averages [65]. In equilibrium, once the system has chosen one of its two possible phases, the relative fluctuations of the magnetization are quite small, and vanish in the thermodynamic limit. This explains the sharp probability density of $S(\vec{q} = 0)$.

In thermal equilibrium above T_c, where the average magnetization is zero, it can be shown relatively easily that

$$\rho(S) = \begin{cases} \frac{1}{\overline{S}} \exp(-\frac{S}{\overline{S}}), \text{ for } \vec{q} \neq 0 \\ \frac{1}{\sqrt{2\pi S\overline{S}}} \exp(-\frac{S}{2\overline{S}}), \text{ for } \vec{q} = 0, \end{cases} \tag{2.36}$$

where $\overline{S}$ is the equilibrium structure factor found in Eq. 2.32. In the derivation of Eq. 2.36 for $\vec{q} = 0$, one uses the facts that the probability density of M is a Gaussian centered at zero, and that $\int_0^\infty \rho(S)dS = \int_{-\infty}^\infty \rho(M)dM$. At $\vec{q} = 0$, this probability distribution has an average $\overline{S}$, and a standard deviation $\sqrt{2}\overline{S}$. Above T_c, the fluctuations of $S(\vec{q})$ do not vanish in the thermodynamic limit.

The previous figures in this section have shown the statistics of the instantaneous scattered intensity, $S(\vec{q}, t)$. In all scattering experiments, the structure factor must be integrated over some exposure time τ, and over some volume in reciprocal space. Both spatial and temporal resolution affect the statistics of the measured intensity.

Let us first study the effect of integrating the scattered intensity over some arbitrary exposure time. The time-averaged structure factor is defined by

$$\overline{S(\vec{q}, t)} = \int_0^\tau S(\vec{q}, t + t')dt'. \tag{2.37}$$

Fig 2.13 shows the ratio of the rms fluctuations of $\overline{S}$, $\sigma_{t,\overline{S}}$, over the ensemble average of $\overline{S}$, $<\overline{S(\vec{q}, t)}>_t$, as a function of q^2 for several τ's. Here the ensemble average of $\overline{S}$ is calculated by

$$<\overline{S(\vec{q}, t)}>_t = \frac{1}{N}\sum_{i=1}^{N} \overline{S(\vec{q}, t_i)}, \tag{2.38}$$

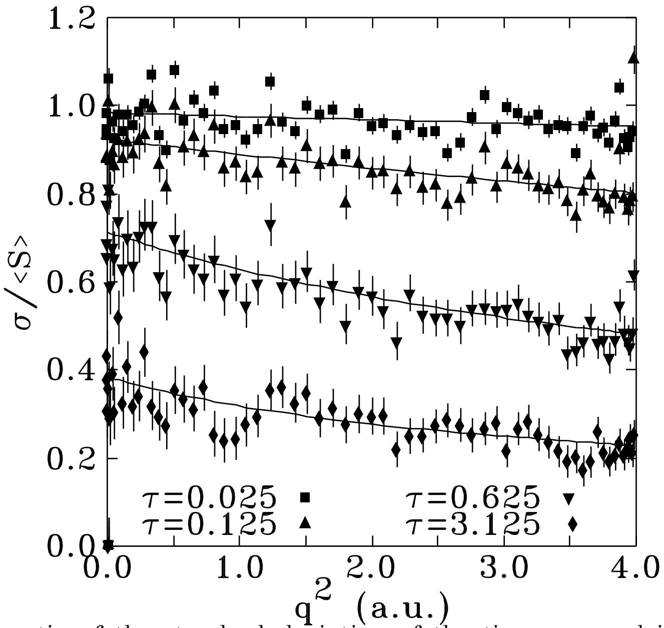

Figure 2.13: The ratio of the standard deviation of the time-averaged intensity $\overline{S}$ over the ensemble average. The data in Fig 2.11b were integrated over different exposure times $\tau = 0.025, 0.125, 0.625, 3.125$. Then $\overline{S}$ was ensemble averaged to calculate its mean and variance. The error bars were calculated with Eq. A.32, derived from standard error analysis.

and the variance of $\overline{S}$, by

$$\sigma^2_{t,\overline{S}} = \frac{1}{N-1} \sum_{i=1}^{N} \left(\overline{S(\vec{q},t_i)} - <\overline{S(\vec{q},t)}>_t \right)^2, \tag{2.39}$$

where $i = 1, 2, 3, ..., N$, and $t_{i+1} - t_i = \tau$. In Fig 2.13, the integration times used to calculate $\overline{S(\vec{q},t)}$ are $\tau = 0.025, 0.125, 0.625, 3.125$.

For small exposure times, $\tau << \tau_c$, the probability density of $\overline{S}$ is nearly equal to the probability density of the instantaneous intensity $S(t)$. This is shown in Fig. 2.13, since $\sigma_{\overline{S}}/<\overline{S}>$ is nearly equal to the ratio for the instantaneous intensity $\sigma_S/<S> = 1$ for the data with $\tau = 0.025$. For larger exposure times the ratio departs from unity, and one can show[1] asymptotically for $\tau >> \tau_c$ that

$$\sigma_{t,\overline{S}}/<\overline{S}>_t \approx \sqrt{2\tau_c/\tau}. \tag{2.40}$$

Note that the ratio $\tau/\tau_c = N_c$, the number of coherence times in one exposure time. Eq. 2.40 states that the second moment of the integrated intensity follows the central limit theorem for large τ, since $\sigma_{t,\overline{S}}/<\overline{S}>_t \propto 1/\sqrt{N_c}$. The solid line in Fig 2.13 is the

[1]The treatment in this section follows closely section 6.1 in Goodman [39]. The factor two in Eq. 2.40 and 2.41 is due to our definition of the correlation time in Fig. 2.11.

exact treatment found in Goodman [39] for a Lorentzian spectrum, valid for any τ, where

$$\frac{\sigma_{t,\overline{S}}}{<\overline{S(\vec{q},t)}>_t} = \left(\frac{2\tau_c}{\tau} + \frac{1}{2}(\frac{2\tau_c}{\tau})^2[\exp(-\tau/\tau_c) - 1]\right)^{\frac{1}{2}}. \tag{2.41}$$

The agreement between the simulation results and Eq. 2.41 is excellent and well within error[1]. The wavevector dependence is due to the q-dependence of the correlation time, which ranges from 0.25 to 0.125 for q^2 between 0 and 4 (see Fig 2.11). Finally, note that the point at the origin is due to the long range order peak which is self-averaging, thus $\sigma/<S> = 0.0$.

Finally, in any coherent scattering experiment, the detector area may average several speckles. This averaging reduces the spatial contrast of the speckle pattern. In section A.1, it is shown that the probability distribution of the spatially averaged scattered intensity sharpens when N speckles are averaged in a given detector area. The resulting spatial contrast of the scattered intensity is reduced from one, for perfect resolution, to $1/\sqrt{N}$ for poorer resolution. Spatial averaging is often used in optics to remove speckle from images obtained by the reflection of light on a rough surface.

[1] Some approximate expressions are derived in the first appendix on how to calculate the error bars for different functions of the estimated mean and variance. Here, the error bars were derived in Eq. A.32. The error bars calculated in Eq. A.32 represent quite accurately the random error caused by evaluating the average and variance with a finite N.